Frontiers in Heat and Mass Transfer

Tech Science Press

https://doi.org/10.32604/fhmt.2026.075018

ARTICLE

Radiative Features of Darcy Forchheimer Flow of Entropy-Optimized Cross Flow Conveying Ternary Hybrid Nanofluid Past a Stretching Cylinder

M. Faizan[1], Syed Sohaib Zafar[2], Farhan Ali[1], Umair Khan[3,4], Aurang Zaib[5] and Najiyah Safwa Khashi'ie[6,*]

[1]Department of Mathematical Sciences, Federal Urdu University of Arts, Sciences & Technology, Gulshan-e-Iqbal, Karachi, Pakistan
[2]Department of Mathematical Sciences, Sir Syed University of Engineering and Technology, Karachi, Pakistan
[3]Department of Mathematics, Saveetha School of Engineering, Saveetha Institute of Medical and Technical Sciences, Saveetha University, Chennai, Tamil Nadu, India
[4]Department of Mathematics, Faculty of Science, Sakarya University, Serdivan, Sakarya, Turkey
[5]Department of Mathematics, University of Karachi, Karachi, Pakistan
[6]Fakulti Teknologi dan Kejuruteraan Mekanikal, Universiti Teknikal Malaysia Melaka, Hang Tuah Jaya, Durian Tunggal, Melaka, Malaysia

*Corresponding Author: Najiyah Safwa Khashi'ie. Email: najiyah@utem.edu.my

Received: 23 October 2025; Accepted: 19 January 2026; Published: 28 February 2026

ABSTRACT: The purpose of the present investigation is to explore the implications of Cross fluid in a Darcy-Forchheimer porous medium due to the tri-hybrid nanofluid past a porous cylinder. Thermal radiation, heat generation, thermal convection, solutal convective and chemical reaction have been encountered in this analysis. Entropy generation has been accounted for under the fluidic friction, heat rate analysis, and porosity analysis. Three different nanoparticles of multiwall carbon nanotube (MWCNT), aluminum oxide (Al_2O_3), and silver (Ag) are utilized to illustrate the tri-hybrid nanofluid flow with Ethlene Glycol (EG) as the base fluid. The governance model, consisting of linked inadequate differential conditions, is transformed into an ordinary configuration of nonlinear coupled differential conditions by acceptable adjustments. The obtained outcomes in combination with the bvp4c approach are then used to resolve the generated ODEs. For discussion purposes, the impacts of the physical limitations on temperature profile, velocity, and concentration have also been illustrated. Numerical results have been obtained for the diffusion rate, heat transfer rate, drag force, and other factors. While the Forchheimer parameter and the inclination angle reduce the fluid flow's velocity, the Biot number of heat and mass transfer influences the fluid's temperature. According to the findings, hybrid nanofluid is the most effective way to improve heat transmission and may also be utilized for cooling. Three different kinds of nanofluids were used in a comparative examination to clarify the study's conclusions. Changes in viscosity and porousness caused the nanofluids' velocity to drop by 13.12% and 15.8%, respectively; however, trihybrid nanofluids with improved convection showed a 13.12% rise.

KEYWORDS: Stretching cylinder; tri-hybrid nanofluid; thermal radiation; cross fluid; heat source/sink

1 Introduction

Several researchers have studied the rate of heat transfer for boundary-layer fluid movement utilizing stretchable cylinders in recent years due to their applicability in engineering and production operations. As a result, Wang [1] demonstrated the surrounding flow of fluid in repose over the initial time using an elastic hollowed cylinder. Stretch cylinders are employed in a variety of uses, including cooling structures, crystal development, wire drawing, electronics device cooling, and paper and glass fiber manufacturing.

Copyright © 2026 The Authors. Published by Tech Science Press. This work is licensed under a Creative Commons Attribution 4.0 International License, which permits unrestricted use, distribution, and reproduction in any medium, provided the original work is properly cited.

Ashraf et al. [2] described the mechanism of magneto magneto-nanofluid of Jeffery flow induced by heat flux Cattaneo Christof upon a stretchable cylinder. Pan et al. [3] explored the mechanism of magneto-bioconvection flow for the Maxwell nanomaterial upon a cylinder using numerical computation. Sadighi et al. [4] discovered the effect of porosity flow on the convective heat through the cylinder via stability analysis. Sudarmozhi et al. [5] deliberated the magneto flow of viscoelastic fluid caused by a gyrating cylinder. Rafique et al. [6] discovered the velocity slip effect and Joule heating on tri-hybrid nanofluid due to stretching a cylinder via numerical simulation. Naveed Khan et al. [7] computed the porosity effect of a hyperbolic tangent nanomaterial past a cylinder with heated convective due to the stratified effect. Mariam et al. [8] explored the consequence of stagnation point flow for convective conditions of Cross hybrid nanoparticles containing aluminium alloy with water as base fluid past a cylinder.

Due to a rising interest in energy utilization and transmission, there has been a significant increase in research on a range of nanofluids during the past few decades. To obtain a large improvement in the transfer of heat rate, Choi and Eastman [9] established the concept of nanofluids, which are formed by adding nanoparticles into ordinary fluids. It has proved useful in a wide range of commercial and technological uses, involving combustion areas, microelectronics, engines for vehicles, and pharmaceutical manufacture. Hybrid nanofluids are more easily detected than individual nanoparticles. Hybrid nanomaterials are created by combining more than two nanoparticles and a liquid. Heating conductivities, temperatures, and molecular density concentrations, in addition to nanoparticle thicknesses and diameters, all contribute to the nanofluid hybrid's thermal endurance. Ogunniyi et al. [10] explored the impact of convective flow on hybrid nanomaterials for the tangential hyperbolic fluid due to the nonlinear thermal radiation. Qin et al. [11] examined the effect of thermal and mass convection of hybrid nanofluid for the Blasius Stokes flow. Mukhtar and Gul [12] simulated the effect of radiative convective flow of a hybridized solar collector. Mebarek-Oudina et al. [13] elaborated on the second law study on the hybrid nanofluid past a porous surface and Lorentz force. Yahaya et al. [14] discussed the irreversibility study of thermal hybridized nanofluid on the static vertical heated convective cone. Ali Shah et al. [15] determined the analytical study of the radiative effect on the hybrid nanofluid with Lorentz force due to an accelerated exponential plate.

Ternary hybrid nanofluids are novel nanomaterials designed to enhance thermal efficiency. Nanofluids, which combine three nanomaterials with a standard liquid, offer superior thermal features as compared to regular liquids. Applications for these materials include contemporary technologies such as solar-powered gadgets for computers, cells for sunlight, sheet making, thermal transfer, thermal thermostatic gadgets, heat exchangers, and refrigeration. Amir et al. [16] elaborated the ramped thermal of tri-hybrid nanomaterial of convective heat flow subject to the Darcy Forchheimer flow using the fractional method. Ramasekhar et al. [17] explained the porosity effect of tri-hybrid nanofluid past a convective heated cylinder. Muhammad Zulfiqar Umer and Ahmad [18] elucidated the features of thermal radiation of tri-hybrid nanofluid due to a stretch surface, considering an artificial neural network. Ouyang et al. [19] illustrated the heated radiated of magnetized tri-hybrid nanofluid with viscous dissipation and convective flow condition through a moving method. Baithalu et al. [20] studied the variable thermal conductivity of tri-hybrid nanofluid of radiative friction force for Marangoni boundary condition. Ighris et al. [21] explicated the buoyancy effect on the irregular chamber for the tri-hybrid nanofluid for the mechanism of the heating process. Mohanty et al. [22] explicated the axisymmetric flow of irreversible analysis of the 3-D structure of tri-hybrid nanofluid using a statistical method. Hussain et al. [23] exhibited the impact of Lorentz force with slippage flow of tri-hybrid nanofluid through a past an exponential sheet. Sohail et al. [24] considered the axisymmetric flow of the buoyancy effect of viscoelastic tri-hybrid nanomaterial, considering the finite element method and porosity effect.

Thermic radiative fluxing is a phenomenon that happens when a surface heats up sufficiently to generate electromagnetic waves, mostly in the infrared region. The friction of the material's atoms and molecules causes this emission. These emitted photons interact with other surfaces via digestion, transmission, or reflection as they carry energy away from them. In practice, thermal radiation is required for a variety of heat transfer applications, including solar energy consumption, thermal control of electronic devices, the development of thermal insulation materials, and heating and cooling systems. A detailed understanding of thermal radiation is required to maximize the efficacy and efficiency of many industrial and technological heat transfer technologies. Asghar et al. [25] conducted a 3-D axisymmetric magnetic flow of heat radiation on the hybrid nanomaterial using a numerical study. Shah et al. [26] illustrated the effect of heat radiation of nanomaterial within a non-Newtonian fluid past a wedge a shape using machine learning. Wahid et al. [27] delineated the buoyancy effect of a hybrid nanofluidic for the heated radiation via a heated convective condition and time-dependent flow. Abdal et al. [28] computed the radiative flow of Maxwell nanomaterial for the bioconvection of heated flux condition. Ahmad et al. [29] expressed the effect of the homogenous and heterogenous reaction on the hybridized nanofluid of the heated radiation via numeric simulation. Salahuddin et al. [30] narrated the stagnant flow of activated energy for the Darcy Forchheimer flow and heated radiation. Sharma et al. [31] traced the mechanism of nanomaterial of viscoelastic flow of heated radiation of irreversibility analysis in solar features. Rehman et al. [32] reported the mechanism of dual diffusive of Reiner-Philippoff of thermal radiation with Darcy Forchheimer flow.

When an impact is applied to the fluid, it causes an alteration in its physical form or framework, which is referred to as distortion. Newtonian and non-Newtonian fluids are elaborated on the relation between the shear rate exerted and deform. Examples include toothbrushes, vinegar colour, blood, and starches. Here are several mathematical models available to investigate the characteristics of non-Newtonian fluids, including the Prandtl, Reiner-Rivlin, Casson, Ree-Eyring, Sisko, and Oldroyd-B models, which do not account for fluid characteristics at different stress rates, among other limitations. Cross [33] exploited the Cross-fluid model to simulate fluid characteristics at different shear rates. Sahu et al. [34] explained the significance of the inertia coefficient of Cross hybridized nanoparticles with a stretching cylinder and mixed convective. Sajid et al. [35] reported the effect of heat generation on the Tiwary-Das model of the Cross-tetra nanoparticles subject to the artery stenosed blood flow and thermal radiation. Mandal and Pal [36] narrated the second law analysis on the Cross hybridized nanomaterial containing GO-Ag/KO past a stretchable sheet with Lorentz force. Jan et al. [37] computed the magnetised Cross tri-hybridised nanomaterial through a porous cylinder through a self-similar solution. Farooq et al. [38] traced the effect of the microorganism of Cross nanomaterial subject to the MHD flow past a stretchable cylinder via a numeric study. Darvesh et al. [39] expressed the impact of Hall ion significance of Cross comprising hybrid nanomaterial past a porous cone through numerical solution. Saleem et al. [40] outlined the mechanism of stratification for the microorganism, Cross radiative flow of nanomaterial.

The existing research highlights an important lack in comprehending the entropy generation for the thermal radiation and heated source/sink on the tri-hybrid nanomaterial via a porous cylinder. The article analyses the flow and heat exchanger properties of Cross tri-hybridised nanomaterial (MWCNT-Al_2O_3-Ag) upon a stretching cylinder with entropy minimization. Tri-hybridised comprises the comprising the multiwall carbon nanotube (MWCNT), aluminum oxide (Al_2O_3), and silver (Ag), along with base fluid ethylene glycol (EG). Heat and mass transports have been computed through thermal and solutal convective conditions. It takes into account the impacts of chemical reaction and thermal radiation to assess their potential for improving thermal and mass performance in industrial uses. Differential expression is considered via the appropriate transformation and the bvp4c technique, provided on the transmuted differential equation. The accuracy of the present technique is tested through contrasting findings with

previously published data. The study examines and addresses how getting factors affect critical flow features like the distribution of temperatures, velocity distribution, Nusselt number, and coefficient of drag at the stretched cylinder. The accuracy of the present technique is tested through contrasting findings with previously published data. The study examines and addresses how getting factors affect critical flow features like the distribution of temperatures, velocity distribution, Nusselt number, and coefficient of drag at the stretched cylinder.

2 Physical Description of the Model Mathematical Formulation

This study examines the radiative flow of Cross fluid with trihybrid nanomaterial ($MWCNT + Al_2O_3 + Ag/EG$) caused by stretching a porous cylinder in the presence of entropy generation. The model has been broadened to incorporate thermal and solutal convective boundary conditions. The Darcy Forchheimer flow has been considered to compute the porosity effect. The current flow configuration includes the chemical species. The flow is measured over a stretchable cylinder. The equations are modeled using cylindrical coordinates (r, z) which can be seen in Fig. 1. In the x and r directions, the velocity components u and v represent that the cylinder of the stretching velocity is $U_w = \frac{U_0 x}{l}$, where the related velocity is denoted by U_0, and the characteristic length is denoted by l. Heat coefficient and temperature of fluid are described by h_f and T_f. The wall concentration is explained by C_w but the far temperature and concentration is examined by T_∞ and C_∞.

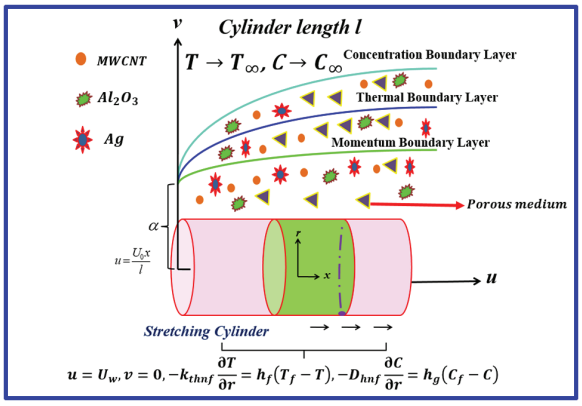

Figure 1: Geometry of the cross darcy forchheimer model of tri-hybrid nanoparticles.

The mathematical models on Cross tri-hybrid for the constitutive equation are (see refs. [35,36]).

$$\frac{\partial(ru)}{\partial x} + \frac{\partial(rv)}{\partial r} = 0, \tag{1}$$

$$u\frac{\partial u}{\partial x} + v\frac{\partial u}{\partial r} = \nu_{thnf}\frac{\partial u}{\partial r}\left[\frac{1}{1+\Gamma\left(\frac{\partial u}{\partial r}\right)^n}\right] + \frac{\nu_{thnf}}{r}\frac{\partial}{\partial r}\left[\frac{\frac{\partial u}{\partial r}}{1+\Gamma\left(\frac{\partial u}{\partial r}\right)^n}\right] - \nu_{thnf}\frac{u}{K} - F_0 u^2, \tag{2}$$

$$u\frac{\partial T}{\partial x} + v\frac{\partial T}{\partial r} - \frac{k_{thnf}}{(\rho C_p)_{thnf}}\left(\frac{\partial^2 T}{\partial r^2} + \frac{1}{r}\frac{\partial T}{\partial r}\right) = \frac{Q_0}{(\rho C_p)_{thnf}}(T - T_\infty) + \frac{1}{(\rho C_p)_{thnf}}\left(\frac{4\sigma^* T_\infty^3}{3k^*}\right)\left(\frac{\partial^2 T}{\partial r^2}\right), \tag{3}$$

$$u\frac{\partial C}{\partial x} + v\frac{\partial C}{\partial y} = D_{thnf}\left(\frac{\partial^2 C}{\partial r^2} + \frac{1}{r}\frac{\partial C}{\partial r}\right) - Kr\,(C - C_\infty)\,. \tag{4}$$

Furthermore, the cross-THNF's thermo-physical properties are distinguished as follows [41]:

$$\frac{\mu_{thnf}}{\mu_f} = \frac{1}{(1-\varrho_1)^{2.5}(1-\varrho_2)^{2.5}(1-\varrho_3)^{2.5}}$$

$$\frac{\rho_{thnf}}{\rho_f} = (1-\varrho_1)\left[(1-\varrho_2)\left\{(1-\varrho_3)+\varrho_3\frac{\rho_3}{\rho_f}\right\}+\varrho_2\frac{\rho_2}{\rho_f}\right]+\varrho_1\frac{\rho_1}{\rho_f}$$

$$\frac{k_{thnf}}{k_{hnf}} = \left(\frac{k_1+2k_{hnf}-2\,\varrho_1\left(k_{hnf}-k_1\right)}{k_1+2k_{hnf}+\varrho_1\left(k_{hnf}-k_1\right)}\right), \frac{k_{hnf}}{k_{nf}} = \left(\frac{k_2+2k_{nf}-2\,\varrho_2\left(k_{nf}-k_2\right)}{k_2+2k_{nf}+\varrho_2\left(k_{NF}-k_2\right)}\right)$$

$$\frac{k_{nf}}{k_f} = \left(\frac{k_3+2k_f-2\,\varrho_3\left(k_f-k_3\right)}{k_3+2k_f+\varrho_3\left(k_f-k_3\right)}\right)$$

$$\frac{(\rho C_p)_{thnf}}{(\rho C_p)_f} = (1-\varrho_1)\left[(1-\varrho_2)\left\{(1-\varrho_3)+\varrho_3\frac{(\rho C_p)_3}{(\rho C_p)_f}\right\}+\varrho_2\frac{(\rho C_p)_2}{(\rho C_p)_f}\right]+\varrho_1\frac{(\rho C_p)_1}{(\rho C_p)_f}$$

$$\frac{D_{thnf}}{D_f} = \left[(1-\varrho_1)^{2.5}(1-\varrho_2)^{2.5}(1-\varrho_3)^{2.5}\right]^{-1}$$

The following is how the boundary constraints are used [26]:

$$u = U_w, v = 0, -k_{thnf}\frac{\partial T}{\partial r} = h_f\left(T_f - T\right), -D_{thnf}\frac{\partial C}{\partial r} = h_g\left(C_f - C\right) \text{ at } r = R \tag{5}$$

$$u \to 0, T \to T_\infty, \mathrm{C} \to C_\infty \text{ as } r \to \infty \tag{6}$$

here, r and z represent the direction with velocity component u, v, the radiative heat flux denotes the q_r, inertia coefficient describes F_0, acceleration due to gravity indicate g, temperature represent T, concentration represent C, heat source describes Q_0, chemical reaction is Kr, Stefan-Boltzmann constant describes σ^*, heat transfer coefficient symbolises h_f, dynamic viscosity represents μ_{thnf}, electric conductivity represents σ_{thnf}, thermal conductivity represents k_{thnf}, density represents ρ_{thnf}, specific heat represents $(\rho c_p)_{thnf}$ of the ternary hybrid nanofluids.

2.1 Thermophysical Properties of the Ternary Hybrid Nanofluids

The tri-hybrid nanofluid employed in this mathematical study is made up of aluminum oxide (Al_2O_3), Multiwall carbon nanotube (MWCNT), Silver (Ag) nanoparticles, and ethylene glycol (EG) as the fundamental based fluid. To create the $MWCNT + Al_2O_3 + Ag$/EG tri-hybrid nanofluid, and then suspended in the preexisting nanofluid combination. ϱ_{MWCNT}, $\varrho_{Al_2O_3}$ and ϱ_{Ag} stand for the solid volume fractions of $MWCNT$, Al_2O_3 and Ag. The correlations of the thermophysical properties (TPPs) of the tri-hybrid nanoliquids are defined in the above section, while physical experimental data of ethylene glycol (EG) and ($MWCNT$, Al_2O_3, Ag) nanoparticles are shown numerically in Table 1. In addition, the detail description of the TPPs correlation used for the nanofluids, hybrid nanofluids, and ternary hybrid nanofluids is given in Table 2.

Table 1: Thermophysical properties of the tri hybrid nanofluid [8,10,17].

Physical Properties	C_p (J/kgK)	ρ (kg/m^3)	k (W/mK)
Ethylene Glycol (EG)	2430	1115	0.25
$MWCNT$	796	1600	3000
Al_2O_3	397.46	3950	12
Ag	235	10,500	429

Table 2: Thermophysical model for ($MWCNT + Al_2O_3 + Ag/EG$).

Properties	$MWCNT/EG$ (Nanofluid)
Dynamics Viscosity (μ)	$\frac{\mu_{nf}}{\mu_f} = \frac{1}{(1-\varrho_1)^{2.5}}$
Density (ρ)	$\frac{\rho_{nf}}{\rho_f} = (1-\varrho_1) + \frac{\varrho_1\rho_{1s}}{\rho_f}$
Thermal conductivity (k)	$\frac{k_{nf}}{k_f} = \frac{k_1+2k_f-2\varrho_1(k_f-k_1)}{k_1+2k_f+\varrho_1(k_f-k_1)}$
Heat Capacity (ρC_p)	$\frac{(\rho c_p)_{nf}}{(\rho c_p)_f} = (1-\varrho_1) + \frac{\varrho_1(\rho c_p)_{1s}}{(\rho c_p)_f}$
Mass diffusivity (D_{nf}))	$D_{nf} = (1-\varrho_1)^{-1}$
Properties	$MWCNT + Al_2O_3/EG$ **(Hybrid nanofluid)**
Viscosity (μ)	$\frac{\mu_{hnf}}{\mu_f} = \frac{1}{(1-\varrho_1)^{2.5}(1-\varrho_2)^{2.5}}$
Density (ρ)	$(1-\varrho_1)\left[(1-\varrho_2)\left\{(1-\varrho_3) + \varrho_3\frac{\rho_3}{\rho_f}\right\} + \varrho_2\frac{\rho_2}{\rho_f}\right] + \varrho_1\frac{\rho_1}{\rho_f}$
Thermal conductivity (k)	$\frac{k_{hnf}}{k_f} = \frac{k_{s1}+2k_{hnf}-2\varrho_1(k_{hnf}-k_1)}{k_{s1}+2k_{hnf}+\varrho_1(k_{hnf}-k_1)} \times \frac{k_{s2}+2k_{nf}-2\varrho_2(k_{nf}-k_{s2})}{k_{s2}+2k_{nf}+\varrho_2(k_{nf}-k_{s2})} k_f$
Heat Capacity (ρC_p)	$\frac{(\rho c_p)_{hnf}}{(\rho c_p)_f} = (1-\varrho_1)\left[(1-\varrho_2) + \frac{\varrho_2(\rho c_p)_{2s}}{(\rho c_p)_f}\right] + \frac{\varrho_1(\rho c_p)_{1s}}{(\rho c_p)_f}$
Mass diffusivity (D_{hnf}))	$D_{hnf} = [(1-\varrho_2)(1-\varrho_2)]^{-1}$
Properties	**(** $MWCNT + Al_2O_3 + Ag/EG$ **) Tri-Hybrid nanofluid**
Viscosity (μ)	$\frac{\mu_{thnf}}{\mu_f} = \frac{1}{(1-\varrho_1)^{2.5}(1-\varrho_2)^{2.5}(1-\varrho_3)^{2.5}}$
Density (ρ)	$\frac{\rho_{thnf}}{\rho_f} = (1-X_1)\left[(1-X_2)\left\{(1-X_3) + \frac{X_3\rho_{2s}}{\rho_f}\right\} + \frac{X_2\rho_{2s}}{\rho_f}\right] + \frac{X_1\rho_{1s}}{\rho_f}$
Thermal conductivity (k)	$\left(\frac{k_1+2k_{hnf}-2\varrho_1(k_{hnf}-k_1)}{k_1+2k_{hnf}+\varrho_1(k_{hnf}-k_1)}\right), \frac{k_{hnf}}{k_{nf}} = \left(\frac{k_2+2k_{nf}-2\varrho_2(k_{nf}-k_2)}{k_2+2k_{nf}+\varrho_2(k_{NF}-k_2)}\right), \frac{k_{nf}}{k_f} = \left(\frac{k_3+2k_f-2\varrho_3(k_f-k_3)}{k_3+2k_f+\varrho_3(k_f-k_3)}\right)$

(Continued)

Table 2 (continued)

Properties	*MWCNT/EG* (Nanofluid)
Heat Capacity (ρC_p)	$\frac{(\rho C_p)_{thnf}}{(\rho C_p)_f} = (1-\varrho_1)\left[(1-\varrho_2)\left\{(1-\varrho_3)+\varrho_3\frac{(\rho C_p)_3}{(\rho C_p)_f}\right\}+\varrho_2\frac{(\rho C_p)_2}{(\rho C_p)_f}\right] + \varrho_1\frac{(\rho C_p)_1}{(\rho C_p)_f}$
Mass diffusion	$\frac{D_{thnf}}{D_f} = \left[(1-\varrho_1)(1-\varrho_2)(1-\varrho_3)\right]^{-1}$

Using the following appropriate transformation,

$$\left.\begin{aligned}\Upsilon = \sqrt{\tfrac{u_0}{\nu L}}\left(\tfrac{r^2-R^2}{2R}\right), U = \tfrac{u_0 x}{L}F'(\Upsilon), v = -\tfrac{R}{r}\sqrt{\tfrac{u_0 \nu}{L}}F(\Upsilon)\\ \Theta(\Upsilon) = \tfrac{T-T_\infty}{T_f-T_\infty}, \Phi(\Upsilon) = \tfrac{C-C_\infty}{C_f-C_\infty}\end{aligned}\right\} \tag{7}$$

Using the transformation of Eqs. (2)–(4) and (7),

$$\varepsilon_1(1+2\varpi\Upsilon)\left[\left(1+(1-n)\left(WeF''\right)^n\right)F'''\right]+2\Gamma F''\left[\left\{1+\left(1-\frac{n}{2}\right)\left(WeF''\right)^n\right\}\right]\varepsilon_1 + \varepsilon_2\left[FF''-F'^2\right]\left\{1+\left(WeF''\right)^n\right\}^2-\left(FrF'^2+KF'\right)\left\{1+\left(WeF''\right)^n\right\}^2=0, \tag{8}$$

$$\Theta''(1+2\varpi\Upsilon)\left(\varepsilon_4+\frac{4}{3}Rd\right)+\frac{1}{\varepsilon_3}PrF\Theta'+Pr\Theta Q=0, \tag{9}$$

$$\phi''(1+2\varpi\Upsilon)+Sc\frac{1}{\varepsilon_5}2\varpi\Upsilon\phi'+Sc\phi'F-ScCe\phi=0. \tag{10}$$

The transformation BCs are articulated:

$$\left.\begin{aligned}F(0)=0, F'(0)=1, \varepsilon_4\Theta'(0)=-Bi\left(1-\Theta(0)\right), \varepsilon_5\phi'(0)=-Bc\left(1-\phi(0)\right)\\ F'(\infty)=0, \Theta(\infty)=0, \phi(\infty)=0.\end{aligned}\right\} \tag{11}$$

The physical features of tri-hybrid nanofluid is given below

$$\varepsilon_1=\frac{\mu_{thnf}}{\mu_f}=\frac{1}{(1-\varrho_1)^{2.5}(1-\varrho_2)^{2.5}(1-\varrho_3)^{2.5}}$$

$$\varepsilon_2=\frac{\rho_{thnf}}{\rho_f}=(1-\varrho_1)\left[(1-\varrho_2)\left\{(1-\varrho_3)+\varrho_3\frac{\rho_3}{\rho_f}\right\}+\varrho_2\frac{\rho_2}{\rho_f}\right]+\varrho_1\frac{\rho_1}{\rho_f}$$

$$\varepsilon_3=\frac{k_{thnf}}{k_{hnf}}=\left(\frac{k_1+2k_{hnf}-2\varrho_1\left(k_{hnf}-k_1\right)}{k_1+2k_{hnf}+\varrho_1\left(k_{hnf}-k_1\right)}\right), \frac{k_{hnf}}{k_{nf}}=\left(\frac{k_2+2k_{nf}-2\varrho_2\left(k_{nf}-k_2\right)}{k_2+2k_{nf}+\varrho_2\left(k_{NF}-k_2\right)}\right)$$

$$\frac{k_{nf}}{k_f}=\left(\frac{k_3+2k_f-2\varrho_3\left(k_f-k_3\right)}{k_3+2k_f+\varrho_3\left(k_f-k_3\right)}\right)$$

$$\varepsilon_4 = \frac{(\rho C_p)_{thnf}}{(\rho C_p)_f} = (1-\varrho_1)\left[(1-\varrho_2)\left\{(1-\varrho_3)+\varrho_3\frac{(\rho C_p)_3}{(\rho C_p)_f}\right\}+\varrho_2\frac{(\rho C_p)_2}{(\rho C_p)_f}\right]+\varrho_1\frac{(\rho C_p)_1}{(\rho C_p)_f}$$

$$\varepsilon_5 = \frac{D_{thnf}}{D_f} = \left[(1-\varrho_1)(1-\varrho_2)(1-\varrho_3)\right]^{-1}$$

Non-dimensionless governing variables are porosity variable $\left(K = \frac{\nu L}{U_0 R^2}\right)$, Weissenberg number $\left(We = \Gamma\frac{Re}{\sqrt{\nu}}\right)$, the inertia coefficient $\left(Fr = \frac{C_b}{k^{1/2}}\right)$, the curvature parameter $\left(\varpi = \left(\frac{\nu}{aR^2}\right)^{1/2}\right)$, Prandtl number $\left(Pr = \frac{\nu}{\alpha}\right)$, radiation parameter $\left(Rd = \frac{4\sigma^* T_\infty^3}{k*k}\right)$, Reynolds number $(Re_x = \frac{U_0 x^2}{\nu L})$, Schmidt number $\left(Sc = \frac{\nu_f}{D_f}\right)$ and chemical reaction parameters $Ce = \left(\frac{K_0 L}{U_0}\right)$.

Drag force, Nusselt and Sherwood number are illustrated as

$$C_f = \left(\frac{\tau_{rx}}{\rho_f u_w^2}\right)_{r=R}, Nu = \left(\frac{x q_w}{k_{thnf}\left(T_f - T_\infty\right)}\right), Sh = \left(\frac{x q_m}{D_{thnf}\left(C_f - C_\infty\right)}\right), \tag{12}$$

The physical quantities of C_f, Nu and Sh are explained by using Eq. (12)

$$\tau_{rr} = \mu_{thnf}\frac{\partial u}{\partial r}\left[\left\{\frac{1}{1+\left(\Gamma\frac{\partial u}{\partial y}\right)^n}\right\}\right], q_w = -k_{thnf}\left(1+\frac{16\sigma^* T_\infty^3}{3k^* k_f}\right)\left(\frac{\partial T}{\partial r}\right), q_m = D_{thnf}\left(\frac{\partial C}{\partial r}\right) \tag{13}$$

Viewing Eqs. (13) in (11)

$$Re^{1/2}C_f = \varepsilon_1 F''(0)\left[\frac{1}{\left\{1+(WeF'')^n\right\}}\right], Re_x^{-1/2}Nu_x = \left[\frac{\boldsymbol{k_{thnf}}}{k_f}+\frac{4}{3}Rd\right]\Theta'(0), Re_x^{-1/2}Sh_x = -\varepsilon_5\phi'(0). \tag{14}$$

2.2 Entropy Generation

The subsequent formula, which captures the complex interaction of the laws of thermodynamics as well as fluid behavior, expresses a volumetric rate at which entropy accumulates inside the setting of the cross trihybrid nanofluid, especially when taking into account the significant effects induced by the presence of the rate of heat, fluid expression, and porosity [42].

$$E_G = \frac{k_f}{T_\infty^2}\left(\frac{\boldsymbol{k_{thnf}}}{k_f}+\frac{16\sigma^* T_\infty^3}{3k^* k_f}\right)\left(\frac{\partial T}{\partial r}\right)^2+\frac{\mu_{thnf}}{T_\infty}\left(\frac{\partial u}{\partial r}\right)^2\left[\frac{1}{1+\Gamma\left(\frac{\partial u}{\partial y}\right)^n}\right]+\frac{\mu_{thnf}}{K}\frac{u^2}{T_\infty} \tag{15}$$

The characteristics of entropy formation is found as

$$Ns(\xi) = Re\left(\frac{k_{thnf}}{k_f}+\frac{4}{3}Rd\right)(1+2\varpi\xi)\Theta'^2+\frac{Br}{\varepsilon_1}(1+2\varpi\Upsilon)\left\{1+\frac{1}{(WeF'')^n}\right\}F''^2+\varepsilon_1 BrKF'^2 \tag{16}$$

Bejan number is explained as

$$Be = \frac{Re\left(\frac{k_{thnf}}{k_f}+\frac{4}{3}Rd\right)(1+2\varpi\Upsilon)\Theta'^2}{\frac{Br}{\varepsilon_1}(1+2\varpi\xi)\left\{1+\frac{1}{(WeF'')^n}\right\}F''^2+\varepsilon_1 BrKF'^2} \tag{17}$$

3 Numerical Computation

Through choosing a suitable conversion and adding pertinent boundary conditions, a set of parametric differential equations is transformed into ODEs, which, using the BVP method called BVP4c, the resulting Eqs. (8)–(10) and the BCs (11) are carried out numerically. The above equations are reformed using freshly established variables into first-order formulations for this study. The flow chart is displayed in Fig. 2.

$$\left.\begin{aligned} F = \mathcal{Q}_1, \mathrm{F}' = \mathcal{Q}_2, \mathrm{F}'' = \mathcal{Q}_3, \mathrm{F}''' = \mathcal{Q}_3' \\ \Theta = \mathcal{Q}_4, \Theta' = \mathcal{Q}_5, \Theta'' = \mathcal{Q}_5' \\ \phi = \mathcal{Q}_6, \phi' = \mathcal{Q}_7, \phi'' = \mathcal{Q}_7' \end{aligned}\right\} \tag{18}$$

$$\mathcal{Q}_3' = \frac{\begin{aligned} -2\varpi\mathcal{Q}_3\left[\left\{1+\left(1-\tfrac{n}{2}\right)(We\mathcal{Q}_3)^n\right\}\right]\varepsilon_1 - \varepsilon_2\left[\mathcal{Q}_1\mathcal{Q}_3 - (\mathcal{Q}_2)^2\right]\left\{1+(We\mathcal{Q}_3)^n\right\}^2 + \\ \varepsilon_3 Fr\{1+(We\mathcal{Q}_3)^n\}^2 \end{aligned}}{\varepsilon_3\,(1+2\varpi\xi)\,(1+(1-n)\,(We\mathcal{Q}_3)^n)} \tag{19}$$

$$\mathcal{Q}_5' = \frac{-\Pr\mathcal{Q}_1\mathcal{Q}_5 - \Pr\mathcal{Q}_4\mathrm{Q}}{(1+2\varpi\xi)\left(\frac{k_{thnf}}{k_f} + \frac{4}{3}Rd\right)} \tag{20}$$

$$\mathcal{Q}_7' = \frac{-2\varpi\mathcal{Q}_7 - \mathrm{Sc}\,(\mathcal{Q}_1\mathcal{Q}_7 - \mathrm{Ce}\mathcal{Q}_6)}{(1+2\varpi\xi)} \tag{21}$$

subject to the BC's

$$\left.\begin{aligned} \mathcal{Q}_1(0) = 0, \mathcal{Q}_2(0) = 1, \mathcal{Q}_5(0) = -\varepsilon_4\,(1-\mathcal{Q}_4(0))\,, \mathcal{Q}_7(0) = -\varepsilon_5\,(1-\mathcal{Q}_6(0)) \\ \mathcal{Q}_2(\infty)\to 0, \mathcal{Q}_4(\infty)\to 0, \mathcal{Q}_6(\infty)\to 0 \end{aligned}\right\} \tag{22}$$

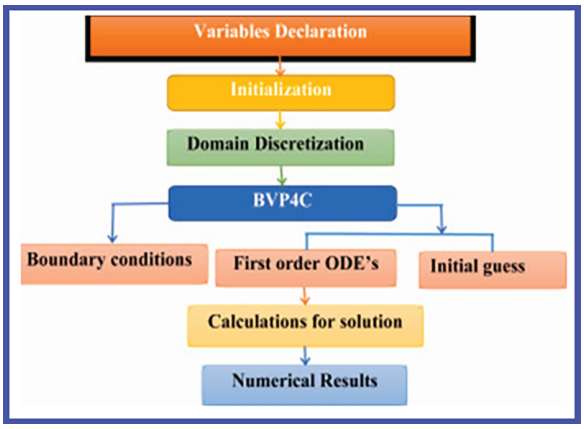

Figure 2: Flow chart of bvp4c.

Finding the missing $F''(0)$, $\Theta'(0)$, and $\phi'(0)$ values required for the equations' resolution is essential to obtaining the numerical simulation of the system described by Eqs. (18)–(22). With ξ_∞ max value of 6, the selected step size was set at 0.001. MATLAB's BVP4c, an integration approach based on the fourth-order Lobatto IIIa formula, was used to numerically solve the boundary value problem. A homogeneous mesh of 60–100 points was used to provide a smooth initial guess. The mesh was automatically improved using BVP4c using residual error estimation. When the collocation residual met the absolute and relative tolerance requirements (AbsTol = 10^{-8}, RelTol = 10^{-6}), convergence was reached. Up until Newton-based iterations

yielded no more improvement, the approach iteratively updated the answer. Without the need for manual tuning, the solver successfully converged for every set of parameters.

4 Results and Discussion

The present part examines the impact of entropy minimization aspects in Cross tri-hybrid nanofluids on the velocity, temperature, and concentration fields. Entropy minimization has been displayed in Figs. 3–8. Furthermore, we existing the variation in drag force, heat/mass transfer via tabular estimation and graphical explanation. This section examines how parameters such as inertia coefficient (Fr), porosity variable (K), thermal radiation parameter (Rd), curvature variable (ϖ), heat source/sink parameter (Q), thermal Biot number (Bi), solutal Biot number (Bc), and chemical reaction (Ce) affect drag coefficient and heat/mass transfer rates for NF, HNF, and THNF cases. When the evaluation, the beliefs of each variable are secured (when the related variable was untouched) as follows: $\varrho_1 = 0.01$, $\varrho_2 = 0.04$, $\varrho_3 = 0.08$, $Fr = 0.2$, $K = 0.2$, $Rd = 0.2$, $Q = 0.4$, $Bi = 0.2$, $Bc = 0.2$, $Sc = 1.0$. Ethylene glycol estimation is set 40.03 for the tri-hybrid nanofluid [43].

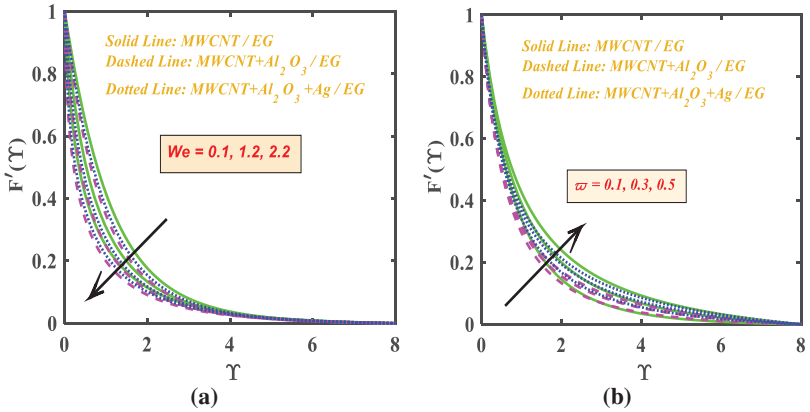

Figure 3: (**a**): We upon $F'(\Upsilon)$; (**b**): ϖ upon $F'(\Upsilon)$.

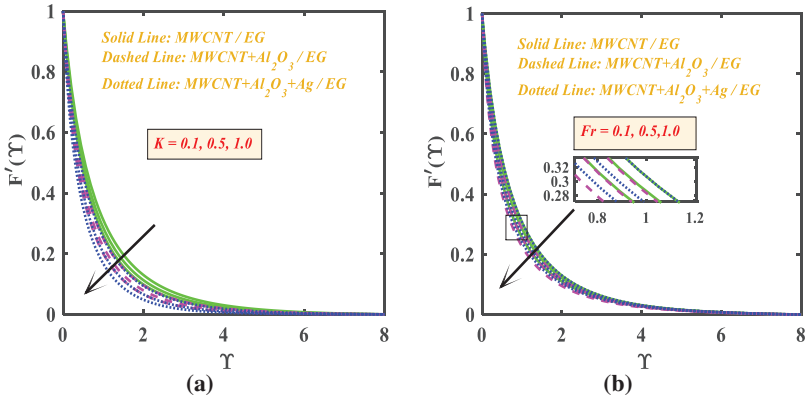

Figure 4: (**a**): K upon $F'(\Upsilon)$; (**b**): Fr upon $F'(\Upsilon)$.

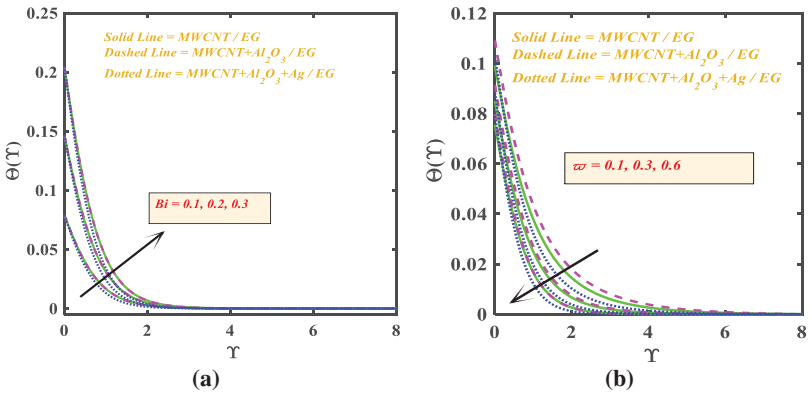

Figure 5: (**a**): Bi upon $\Theta(\Upsilon)$; (**b**): ϖ upon $\Theta(\Upsilon)$.

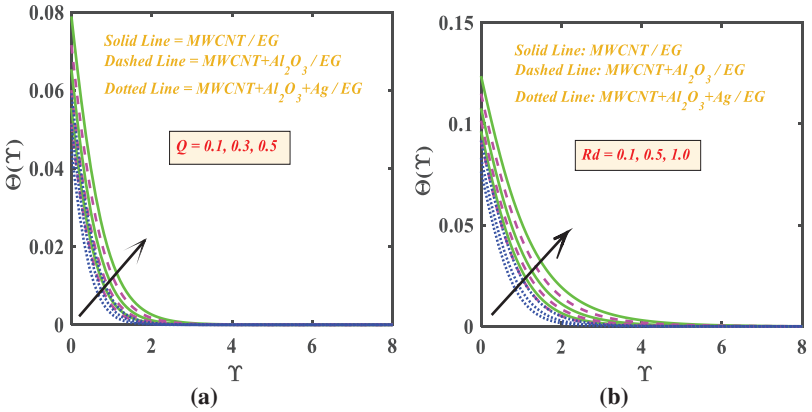

Figure 6: (**a**): Q upon $\Theta(\Upsilon)$; (**b**): Rd upon $\Theta(\Upsilon)$.

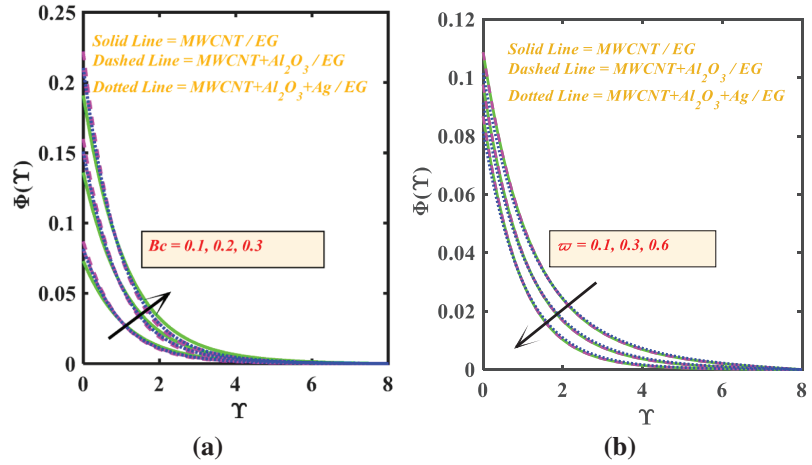

Figure 7: (**a**): Bc upon $\Phi(\Upsilon)$; (**b**): ϖ upon $\phi(\Upsilon)$.

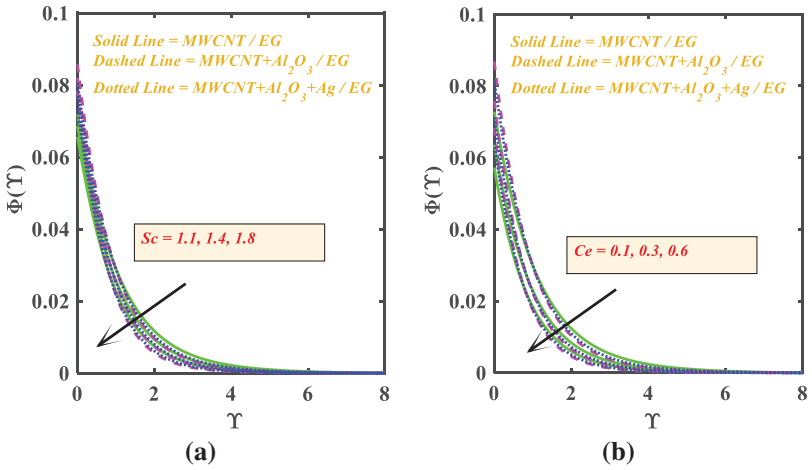

Figure 8: (**a**): Sc upon $\phi(\Upsilon)$; (**b**): Ce upon $\phi(\Upsilon)$.

The consequences of the velocity distribution $F'(\Upsilon)$ upon the Weissenberg number (We) and curvature parameter (ϖ) for three distinct nanomaterial combinations are exposed in Fig. 3a,b. Fig. 3a displays that the larger estimation of Weissenberg number (We) declined the velocity distribution $F'(\Upsilon)$ for distinct of nanoparticles. Physically, it measures how strong elastic forces are in relation to strain rates in a velocity field. Fig. 3b explains that the greater magnitude of curvature parameter (ϖ) escalates the velocity distribution $F'(\Upsilon)$. Therefore, larger curvature indicates greater flow of fluid in velocity profiles, which is the effect of the curvature parameter.

Fig. 4a,b exhibits the significance of porosity variable (K) and inertia coefficient (Fr) for three distinct nanoparticles ($MWCNT + Al_2O_3 + Ag$). Fig. 4a reveals that the augmentation in the porosity variable (K) depreciates the velocity distribution $F'(\Upsilon)$. The velocity distribution within and around a permeable cylinder is greatly influenced by the porous variable, which is frequently connected to the porosity. The fluid flow or penetration through a porous cylinder is controlled by the porous parameter. The reducing outcomes for the larger estimation against velocity distribution $F'(\Upsilon)$ for the scenario of the tri-hybrid nanofluid ($MWCNT + Al_2O_3 + Ag$). Physically, in porosity stream models, a regressive obstacle is introduced via the inertia coefficient. It is crucial in flows of dense, low-porosity, or high-speed media.

Fig. 5a,b establishes the mechanism of thermal Biot number (Bi) and curvature variable (ϖ) upon the thermal distribution $\Theta(\Upsilon)$ due to the $MWCNT + Al_2O_3 + Ag$ with base fluid EG. Fig. 5a develops the thermal distribution $\Theta(\Upsilon)$ pattern grows with growing estimates of Bi, and a high Biot number denotes a higher cylinder internal thermal resistance relative to the boundary layer thermal resistance. Fig. 5b illustrates how the temperature curve declines as curvature factors (ϖ) rise. It is frequently described as a ratio between a boundary layer thickness or streamwise coordinate and a characteristic length scale of curvature (such as radius), and it indicates the degree to which the outermost layer deviates from a flat plane. The addition of curvature (such as flow across a cylinder or sphere) results in larger temperature gradients than flat-plate Blasius flow because of the augmented velocity field that draws heat farther from the surface. Fig. 6a,b indicates that the thermal distribution $\Theta(\Upsilon)$ due to the $MWCNT + Al_2O_3 + Ag$ with base fluid EG for the heat source/sink (Q) and thermal radiation (Rd). Fig. 6a depicts that the thermal distribution $\Theta(\Upsilon)$ enhanced as the heat source sink (Q) is augmented. The temperature profile of the flow is considerably altered when a heat source or sink is present in a thermal boundary layer. Fig. 6b views the thermal radiation (Rd) enhances the the thermal distribution $\Theta(\Upsilon)$. Thermal radiation is the production

of electromagnetic radiation as a result of the temperature of an object. The radiation characteristics are influenced by the thermal profile, which is the spatial distribution of temperature in a system.

Fig. 7a,b displays the significance of solutal Biot number (Bc) and curvature variable (ϖ) upon the concentration distribution $\phi(\Upsilon)$ $MWCNT + Al_2O_3 + Ag$ with base fluid EG. Fig. 7a found that the concentration distribution $\phi(\Upsilon)$ implies an accelerating estimation of solutal Biot number (Bc). In mass transfer requiring concentration boundary layers, the solutal Biot number is crucial, particularly when a body has both internal and external diffusion resistance. Fig. 7b reveals the deprecating phenomena for the augmenting magnitude of curvature variable (ϖ). A thicker layer of concentration results in a reduced gradient of surface concentration and diminished mass flow. The Schmidt number (Sc) influence is seen in Fig. 8a. Al_2O_3 reductions more quickly than $MWCNT$ nanofluid because the concentration profile is delayed as the diffusion coefficient rises and the mass transfer rate decreases. Fig. 8b displays a graphical depiction of the chemical reaction parameter (Ce). The graphic clearly shows that when the chemical reaction parameter (Ce) rises, the concentration profile rapidly decreases. This is consistent with the physical fact that, for $MWCNT + Al_2O_3 + Ag$ tri-hybrid nanofluids, high molecular motion results in a higher mass transportation process, which delays the fluid concentration profile.

The entropy generation $Ns(\Upsilon)$ for the numerous estimations of the Weissenberg variable We is illustrated in Fig. 9a. Enhancing the magnitude of the Weissenberg number (We), the entropy generation $Ns(\Upsilon)$ reveals the depreciating phenomena. The production of entropy is significantly influenced by the Weissenberg number (We), particularly in flows involving viscoelastic fluids. Fig. 9b elucidates the role of radiative variable (Rd) on the entropy generation $Ns(\Upsilon)$. The rapid enhancement in the entropy generation $Ns(\Upsilon)$ due to the greater values of the radiative variable (Rd). The transmission of energy via electromagnetic waves as a result of body temperature is known as thermal radiation. The entropy generation $Ns(\Upsilon)$ for the numerous estimations of Weissenberg number (We) is illustrated in Fig. 10a. Enhancing the magnitude of the Weissenberg number We the entropy generation $Ns(\Upsilon)$ reveals the depreciating phenomena. The production of entropy is significantly influenced by the Weissenberg number (We), particularly in flows involving viscoelastic fluids. Porosity effect (K) has been incorporated in Fig. 10b. A declined in the Entropy generation $Ns(\Upsilon)$ is noted for the flow region due to the larger estimation of the porous variable (K).

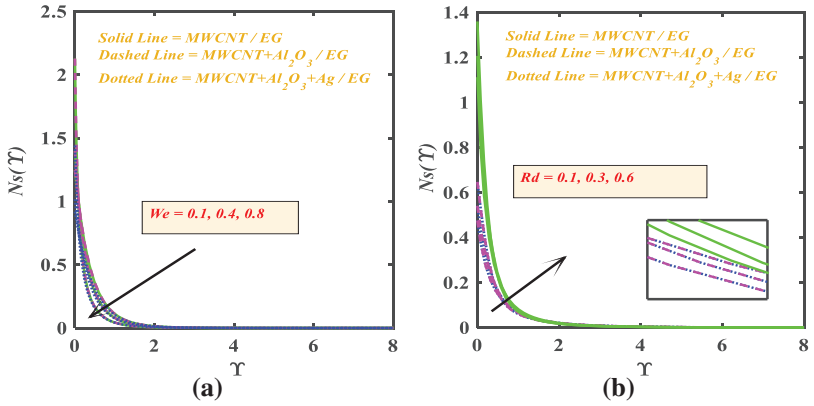

Figure 9: (**a**): We upon $Ns(\Upsilon)$; (**b**): Rd upon $Ns(\Upsilon)$.

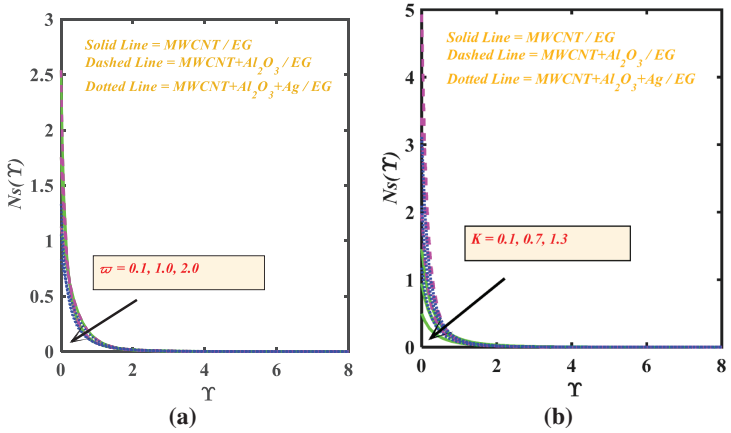

Figure 10: (**a**): ϖ upon $Ns(\Upsilon)$; (**b**): K upon $Ns(\Upsilon)$.

The effect of the Weissenberg variable (We) for the Bejan number $Be(\Upsilon)$ has been seen in Fig. 11a. A bigger estimation of the Weissenberg variable (We) reduces the Bejan number (Be). In viscoelastic fluid flows, the Weissenberg number (We) modifies the flow and stress fields, which in turn influences the Bejan number Bejan number $Be(\Upsilon)$. The interaction can drastically alter the entropy balance since the Weissenberg number provides elasticity effects, and the Bejan number quantifies the proportional relevance of heat transfer irreversibility to overall entropy creation. It is clear from Fig. 11b that the Bejan number accelerates as the radiation parameter (Rd) escalates. The proportional contributions of heat transfer irreversibility and fluid friction irreversibility to entropy formation are measured by the dimensionless Bejan number. The inclusion of thermal radiation modifies gradients of temperature, which in turn influences heat transfer-induced creation of entropy and, consequently, the Bejan number. The role of curvature variable (ϖ) vs. the variation of Bejan number $Be(\Upsilon)$ is seen in Fig. 12a. The process will be more chaotic the less the Bejan number $Be(\Upsilon)$. The impact of the amount of porous variable upon the Bejan number is shown in Fig. 12b. We note that an increase in the Bejan number $Be(\Upsilon)$ corresponds to a decrease in the Bejan number $Be(\Upsilon)$. This suggests that the Bejan number caused by irreversibility, particularly porosity drag, gets more prominent as the cylinder gets thinner in comparison to the irreversibility caused by the transfer of heat.

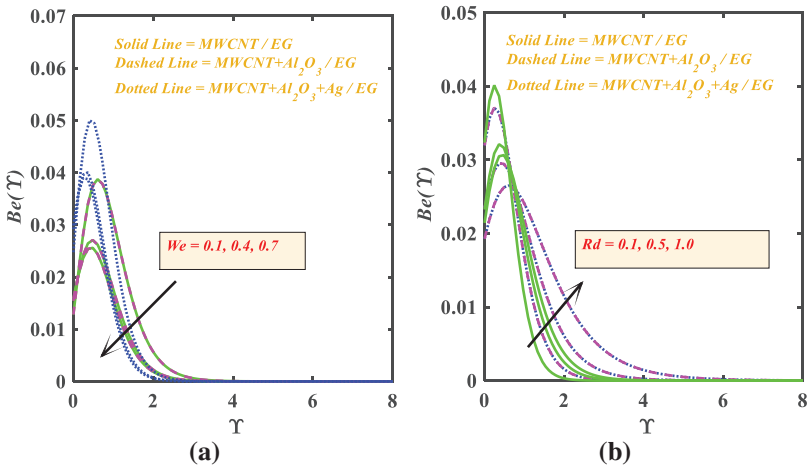

Figure 11: (**a**): We upon $Be(\Upsilon)$; (**b**): Rd upon $Be(\Upsilon)$.

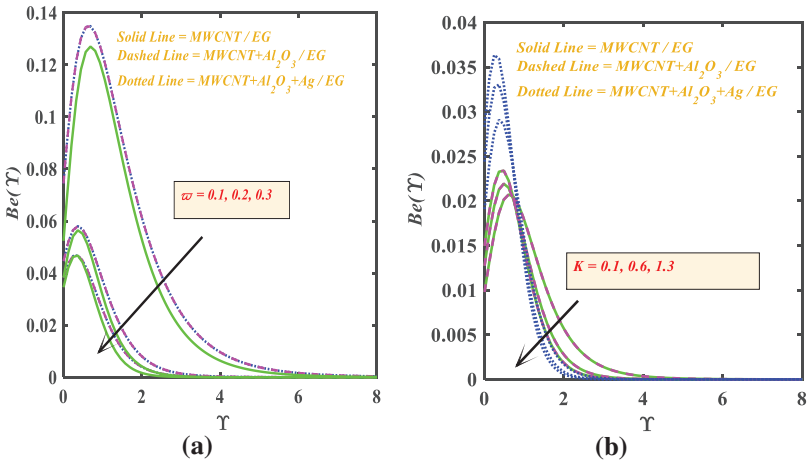

Figure 12: (**a**): ϖ upon $Be(\Upsilon)$; (**b**): K upon $Be(\Upsilon)$.

Fig. 13a–c shows the contour for the tri-hybrid nanofluid, hybrid, and nanofluid. Fig. 14a–c reveals the drag force C_f, Nusselt number Nu, and Sherwood Sh against We, Fr, Rd, Bi, Sc, and Ce. Fig. 15a–c views that the grid analysis for the velocity, temperature, and concentration fields for the sizes of 100, 150, and 200. Table 3 shows the drag force for the various values of We, Fr, K and n. Larger values of We, Fr, K accelerate the drag force, while the opposite effect is examined for the n. Table 4 reveals the greater Nusselt number for the bigger estimation of Bi, Rd, Q while the Nusselt number is depreciated for the ϖ. Table 5 exhibits the effect of Sherwood number for the values of Bc, Sc, Ce, and ϖ. Augmented in the Sherwood number for the larger values Sc, Ce, ϖ but depreciation for the Bc. Tables 6 and 7 show the comparison of Rd and curvature variable with previous literature, and found an excellent agreement. Table 8 reveals the different values of h for the grid analysis for the $F'(\Upsilon), \Theta(\Upsilon)$ and $\phi(\Upsilon)$.

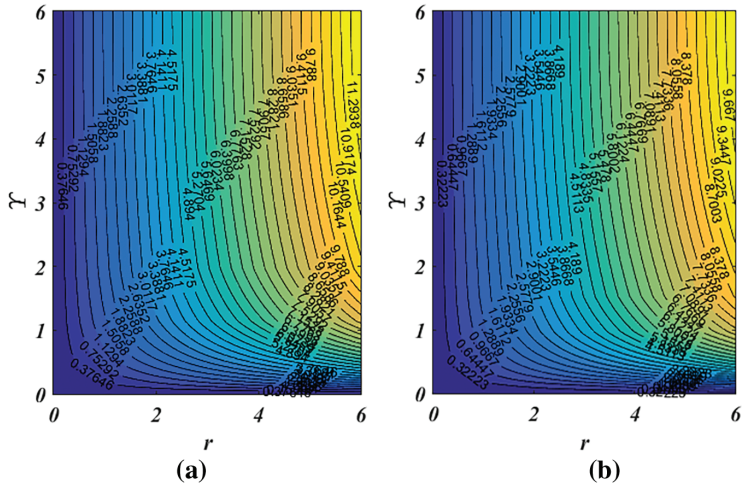

Figure 13: (Continued)

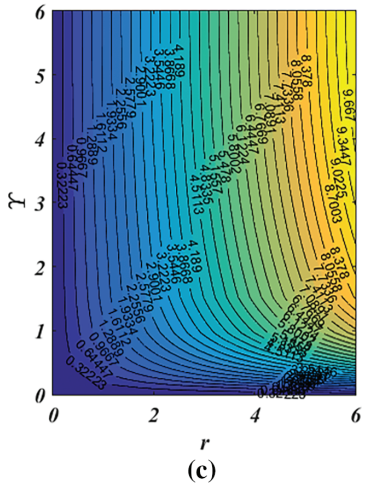

(c)

Figure 13: (**a**): Tri-hybrid nanofluid ($MWCNT + Al_2O_3 + Ag$/EG); (**b**): Hybrid nanofluid ($MWCNT + Al_2O_3$/EG); (**c**): Nanofluid ($MWCNT$/EG).

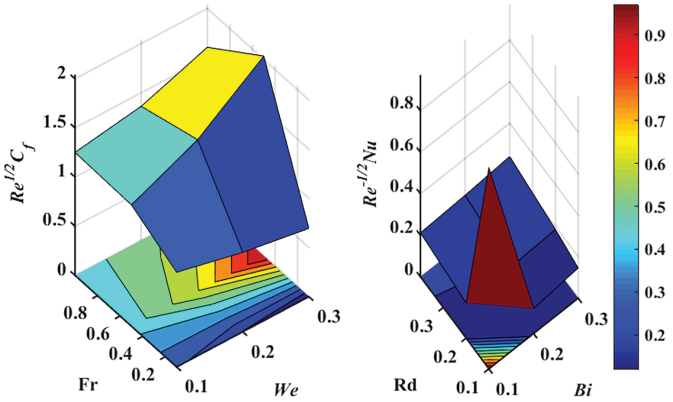

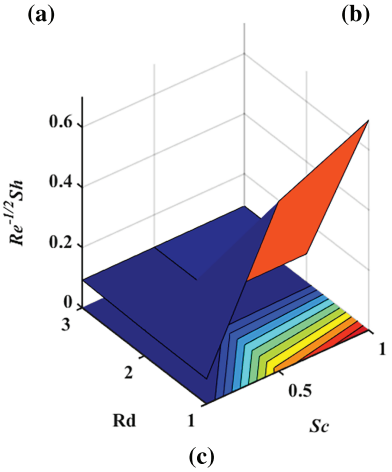

Figure 14: (**a**): C_f against We and Fr; (**b**): Nu against Rd and Bi; (**c**): Sh against Rd and Sc.

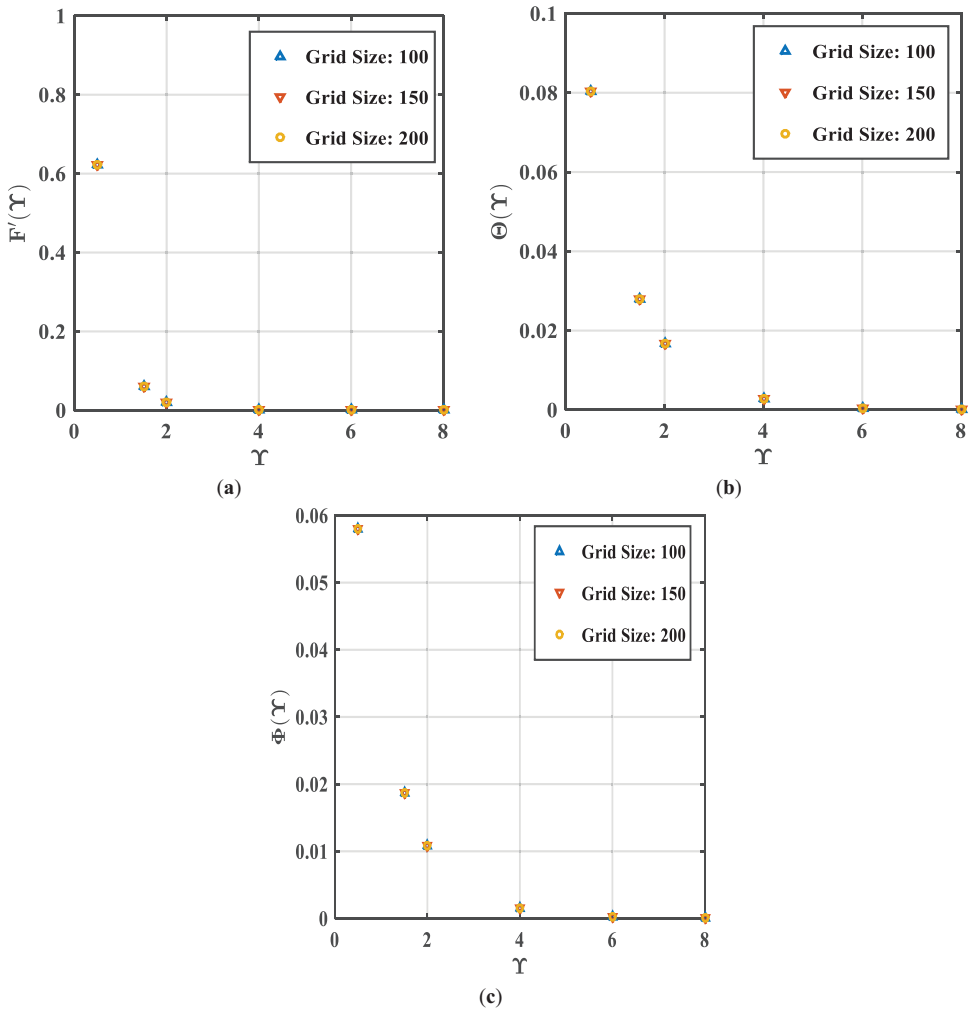

Figure 15: (**a**): Grid analysis for the $F'(\Upsilon)$; (**b**): Grid analysis for the $\Theta(\Upsilon)$; (**c**): Grid analysis for the $\phi(\Upsilon)$.

Table 3: Drag force for the numerous estimations of We, n, Fr and K.

				Cf		
We	n	Fr	K	$MWCNT/EG$	$MWCNT + Al_2O_3$ /EG	$MWCNT + Al_2O_3 + Ag/EG$
0.1				1.2349	1.2452	1.2567
0.2				1.5401	1.5510	1.5620
0.3				2.0339	2.0749	2.1061
	1.0			0.9627	0.9723	0.9853
	2.0			0.8080	0.8183	0.8245
	3.0			0.6945	0.7050	0.7153
		0.1		1.2509	1.2702	1.2943
		0.5		1.3625	1.3867	1.4078
		1.0		1.6055	1.6119	1.6389
			0.1	0.9814	0.9910	1.0021

(Continued)

Table 3 (continued)

				Cf		
We	n	Fr	K	$MWCNT/EG$	$MWCNT + Al_2O_3$ /EG	$MWCNT + Al_2O_3 + Ag/EG$
			0.5	1.0913	1.1024	1.1145
			1.0	1.3245	1.3456	1.3649

Table 4: Numerical values of Nusselt number for the numerous estimations of Bi, Rd, Q and ϖ.

				Nu		
Bi	Rd	Q	ϖ	$MWCNT/EG$	$MWCNT + Al_2O_3$ /EG	$MWCNT + Al_2O_3 + Ag/EG$
0.1				0.2443	0.2545	0.2673
0.2				0.4545	0.4632	0.4787
0.3				0.6373	0.6490	0.6589
	1.0			0.0969	0.0970	0.0983
	2.0			0.1211	0.1321	0.1211
	3.0			0.1454	0.1504	0.1660
		0.1		0.1697	0.1701	0.1710
		0.5		0.1718	0.1801	0.1810
		1.0		0.1834	0.1903	0.1910
			0.1	0.2314	0.2418	0.2565
			0.5	0.2228	0.2332	0.2454
			1.0	0.2195	0.2299	0.2356

Table 5: Numerical values of Sherwood number for the numerous estimations of Bc, Ce, Sc and ϖ.

				Sh		
Bc	Ce	Sc	ϖ	$MWCNT/EG$	$MWCNT + Al_2O_3$ /EG	$MWCNT + Al_2O_3 + Ag/EG$
0.1				0.0828	0.0829	0.0830
0.2				0.5644	0.5747	0.5852
0.3				0.6982	0.7084	0.7190
	1.0			0.0851	0.0852	0.0853
	2.0			0.0926	0.0927	0.0928
	3.0			0.0938	0.0939	0.0940
		0.1		0.0920	0.0921	0.0922
		0.5		0.0925	0.0926	0.0927
		1.0		0.0933	0.0934	0.0936
			0.1	0.0929	0.0930	0.0932
			0.5	0.0854	0.0855	0.0858
			1.0	0.0816	0.0818	0.0820

Table 6: Comparison of *Rd* for the drag force and Nusselt number.

Rd	$F''(0)$	$\Theta'(0)$	$F''(0)$	$\Theta'(0)$
	Hussain et al. [42]		**Current Studies**	
1	1.4159	0.7184	1.41592541	0.718414983
2	1.4452	0.8845	1.44525482	0.884524516

Table 7: Comparison of ϖ for the drag force.

ϖ	**Rangi and Ahmad [43]**	**Current Result**
0	1.0000	1.0001
0.25	1.0943	1.0921
0.5	1.1897	1.1819
0.75	1.2818	1.2890
1	1.4593	1.4562

Table 8: Grid analysis for the $F'(\Upsilon)$, $\Theta(\Upsilon)$ and $\phi(\Upsilon)$ for the size of 100, 150 and 200.

Function	*h*	ζ					
		0.5	**1.5**	**2.0**	**4.0**	**6.0**	**8.0**
$F'(\Upsilon)$	100	0.6223	0.0612	0.0214	0.0006	0.00	0.000
	150	0.4845	0.0940	0.0430	0.0028	0.0003	0.0000
	200	0.0375	0.0098	0.0055	0.0008	0.0002	0.0000
$\Theta(\Upsilon)$	100	0.0365	0.0029	0.002	0.0000	0.0000	0.0000
	150	0.0802	0.0279	0.0167	0.0027	0.0005	0.0000
	200	0.6322	0.0732	0.0288	0.0013	0.0001	0.0000
$\phi(\zeta)$	100	0.0376	0.0083	0.0041	0.0004	0.0000	0.0000
	150	0.0579	0.0187	0.0109	0.0016	0.0003	0.0000
	200	0.0461	0.0123	0.0069	0.0011	0.0002	0.000

5 Conclusions

This research examines the Darcy-Forchheimer flow Cross Tri-hybrid nanoparticles upon a stretchable cylinder, taking into account the second law analysis. Thermal radiation, heat source/sink, and chemical reaction have been assumed. Thermal and solutal convective conditions have been used to compute the heat and mass. Multiwall carbon nanotube (MWCNT), aluminum oxide Al_2O_3, and silver Ag have been assumed. The study examines the entropy generation, Bejan number, velocity, and temperature distribution of Multiwall carbon nanotube (MWCNT), aluminum oxide Al_2O_3, and silver Ag nanoparticles under various conditions. We analyzed the thermal radiation, heat source/sink, and chemical reaction over a stretched cylinder. The bvp4c approach was used to get solutions. We utilized the bvp4c approach and found great agreement between their results. Our findings show that in the presence of a porous media, the tri-hybrid nanoliquid exhibits exceptional thermal characteristics. This model's key results are:

- The greater the curvature parameter leads the enhanced the velocity field for the $MWCNT + Al_2O_3 + Ag$/EG.
- The velocity field is reduced due to the increasing inertia coefficient, porous variable, and Weissenberg number for the $MWCNT + Al_2O_3 + Ag$/EG.
- The $MWCNT + Al_2O_3 + Ag$/EG hybrid nanofluid has a higher maximum temperature distribution for the Biot number, thermal radiation, and heat source/sink.
- The $MWCNT + Al_2O_3 + Ag$/EG hybrid nanofluid has a higher maximum temperature distribution for the Biot number, thermal radiation, and heat source/sink.
- The chemical reaction (Ce) and the Schmidth number (Sc) depreciates the concentration of $MWCNT + Al_2O_3 + Ag$/EG.
- The porosity effect reduces the entropy production and Bejan number for the scenario of $MWCNT + Al_2O_3 + Ag$/EG.

The main limitation of the temperature-independent thermophysical properties; this limits accuracy at very large temperature differences.

Acknowledgement: The authors acknowledge Universiti Teknikal Malaysia Melaka for the research support through grants ANTARABANGSA(IRMG)-TEL-U/2025/FTKM/A00086.

Funding Statement: This research was funded by Universiti Teknikal Malaysia Melaka.

Author Contributions: The authors confirm contribution to the paper as follows: study conception and mathematical formulation: M. Faizan, Syed Sohaib Zafar, Farhan Ali, Umair Khan; data collection: M. Faizan, Syed Sohaib Zafar, Farhan Ali, Umair Khan, Aurang Zaib; analysis and interpretation of results: Farhan Ali, Umair Khan, Aurang Zaib, Najiyah Safwa Khashi'ie; draft manuscript preparation: M. Faizan, Syed Sohaib Zafar, Farhan Ali, Umair Khan, Aurang Zaib, Najiyah Safwa Khashi'ie. All authors reviewed and approved the final version of the manuscript.

Availability of Data and Materials: All data are available within the manuscript.

Ethics Approval: Not applicable.

Conflicts of Interest: The authors declare no conflicts of interest.

Nomenclature

Bi	Biot number (-)
Bc	Mass biot number (-)
Be	Bejan rate (-)
Br	Brikman number (-)
C	Concentration (kmolm^{-3})
C_f	Convective surface
C_∞	Ambient concentration
C_ρ	Is the heat capacity ($\text{Jkg}^{-1}\text{K}^{-1}$)
Ce	Chemical reaction rate
Fr	Inertia coefficient
K	Porosity parameter (-)
Q	Heat source/sink (-)
Rd	Radiation term (-)
$Re_r^{1/2}C_f$	Skin friction (-)
$Re_r^{-1/2}Nu$	Nusselt number (-)
$Re_r^{-1/2}Sh$	Sherwood number (-)

Sc	Schmidth number (-)
T	Fluid temperature (K)
T_f	Convective fluid temperature (-)
T_∞	Surface and ambient temperature (-)
We	Weissenberg number (-)

Greek Symbol

Γ	Material constant time (-)
ϖ	Curvature variable (-)
ε_1	Temperature ratio parameter
$\boldsymbol{\mu_{thnf}}$	Dynamic viscosity of tri-hybrid nanofluid ($kgm^{-1}s^{-1}$)
k^*	Mean absorption (m^{-1})
σ^*	Stefan-Boltzmann ($Wm^{-2}K^{-4}$)
k_{thnf}	Heat Conductivity
$\boldsymbol{\rho_{thnf}}$	Density of tri-hybrid nanofluid (kg/m^3)
ν_{thnf}	Kinematic viscosity (ms^{-1})

References

1. Wang CY. Fluid flow due to a stretching cylinder. Phys Fluids. 1988;31(3):466–8. doi:10.1063/1.866827.
2. Ashraf MB, Rafiullah, Tanveer A, Ulhaq S. Effects of Cattaneo-Christov heat flux on MHD Jeffery nano fluid flow past a stretching cylinder. J Magn Magn Mater. 2023;565:170154. doi:10.1016/j.jmmm.2022.170154.
3. Pan H, Yousaf A, Imran M, Tahir M, Farooq U. Numerical simulation of Maxwell nanofluid with MHD and bio-convective flow passing through a stretching cylinder. Int J Thermofluids. 2023;20:100423. doi:10.1016/j.ijft.2023.100423.
4. Sadighi S, Afshar H, Ashtiani HAD, Jabbari M. MHD flow and conductive heat transfer on a permeable stretching cylinder: benchmark solutions. Case Stud Therm Eng. 2023;44:102886. doi:10.1016/j.csite.2023.102886.
5. Sudarmozhi K, Iranian D, Khan I. Heat and mass transport of MHD viscoelastic fluid flow towards a permeable stretching cylinder. Int Commun Heat Mass Transf. 2023;145:106864. doi:10.1016/j.icheatmasstransfer.2023.106864.
6. Rafique K, Mahmood Z, Usman A, Farooq U, Emam W. Numerical study of MHD flow over stretching cylinder with variable Prandtl number and viscous dissipation in ternary hybrid nanofluids with velocity and thermal slip conditions. Mod Phys Lett B. 2025;39(11):2450465. doi:10.1142/s0217984924504657.
7. Naveed Khan M, Alhowaity A, Wang Z, Gepreel KA, Hussien M. Numerical analysis of the heat transfer application on a convective tangent hyperbolic nanofluid flow over a porous stretching cylinder with stratification effects. Numer Heat Transf Part A Appl. 2025;86(21):7705–21. doi:10.1080/10407782.2024.2353881.
8. Mariam A, Salamat N, Abdal S, Hussain S, Siddique I, Yaseen ZM, et al. Enhancing thermal transport in industrial applications: a study on AA7072–AA7075 hybrid nanofluid over a stretching cylinder with MHD and heat source/sink effects. Proc Inst Mech Eng Part N J Nanomater Nanoeng Nanosyst. 2025;19:1492. doi:10.1177/23977914251356729.
9. Choi SUS, Eastman JA. Enhancing thermal conductivity of fluids with nanoparticles. Lemont, IL, USA: Argonne National Lab (ANL); 1995.
10. Ogunniyi PO, Gbadeyan AJ, Agarana MC, Yusuf TA. Nonlinear thermal radiation on MHD tangential hyperbolic hybrid nanofluid over a stretching wedge with convective boundary condition. Heat Transf. 2022;51(6):5417–40. doi:10.1002/htj.22553.
11. Qin L, Ahmad S, Khan MN, Ahammad NA, Gamaoun F, Galal AM. Thermal and solutal transport analysis of Blasius-Rayleigh-Stokes flow of hybrid nanofluid with convective boundary conditions. Waves Random Complex Medium. 2025;35(3):5615–33. doi:10.1080/17455030.2022.2072018.
12. Mukhtar S, Gul T. Solar radiation and thermal convection of hybrid nanofluids for the optimization of solar collector. Mathematics. 2023;11(5):1175. doi:10.3390/math11051175.

13. Mebarek-Oudina F, Chabani I, Vaidya H, Ismail AAI. Hybrid-nanofluid magneto-convective flow and porous media contribution to entropy generation. Int J Numer Meth Heat Fluid Flow. 2024;34(2):809–36. doi:10.1108/hff-06-2023-0326.
14. Yahaya RI, Mustafa MS, Arifin NM, Pop I, Wahid NS, Ali FM, et al. Mixed convection hybrid nanofluid flow over a stationary permeable vertical cone with thermal radiation and convective boundary condition. Z Angew Math Mech. 2024;104(4):e202300428. doi:10.1002/zamm.202300428.
15. Ali Shah N, Ali F, Yook SJ, Faizan M, Zafar SS, Sidi MO. Dynamics of chemical reactive on magneto Hybrid Nanomaterial with heat radiation due to porous exponential plate: laplace transform technique for the heat and mass. J Radiat Res Appl Sci. 2025;18(1):101295. doi:10.1016/j.jrras.2025.101295.
16. Amir M, Ali Q, Raza A, Almusawa MY, Hamali W, Ali AH. Computational results of convective heat transfer for fractionalized Brinkman type tri-hybrid nanofluid with ramped temperature and non-local kernel. Ain Shams Eng J. 2024;15(3):102576. doi:10.1016/j.asej.2023.102576.
17. Ramasekhar G, Divya A, Jakeer S, Reddy SRR, Algehyne EA, Jawad M, et al. Heat transfer innovation of engine oil conveying SWCNTs-MWCNTs-TiO_2 nanoparticles embedded in a porous stretching cylinder. Sci Rep. 2024;14:16448. doi:10.1038/s41598-024-65740-8.
18. Muhammad Zulfiqar Umer C, Ahmad I. Intelligent computing applications to study the tri-hybrid nanofluid past over the stretched surface. Results Phys. 2024;65:107972. doi:10.1016/j.rinp.2024.107972.
19. Ouyang Y, Md Basir MF, Naganthran K, Pop I. Unsteady magnetohydrodynamic tri-hybrid nanofluid flow past a moving wedge with viscous dissipation and Joule heating. Phys Fluids. 2024;36(6):062009. doi:10.1063/5.0208608.
20. Baithalu R, Mishra SR, Panda S. Marangoni convection with variable thermal conductivity and impact of inertial drag on radiative tri-hybrid nanofluid flow over a Riga plate with non-uniform heat emission/release. J Therm Anal Calorim. 2024;149(24):15291–304. doi:10.1007/s10973-024-13766-5.
21. Ighris Y, Qaffou M, Baliti J, Elguennouni Y, Hssikou M. Thermal management optimization of natural convection in a triangular chamber: role of heating positions and ternary hybrid nanofluid. Phys Fluids. 2024;36(9):092002. doi:10.1063/5.0226427.
22. Mohanty D, Mahanta G, Shaw S, Katta R. Entropy and thermal performance on shape-based 3D tri-hybrid nanofluid flow due to a rotating disk with statistical analysis. J Therm Anal Calorim. 2024;149(21):12285–306. doi:10.1007/s10973-024-13592-9.
23. Hussain SM, Mishra MK, Alraddadi I, Al-Luhaybi IAM. Thermal analysis of trihybrid ($Co+ZrO_2+Au/H_2O$) nanofluid flow through the exponentially deformable surface with Lorentz force and Navier's slippage constraint. Int J Numer Meth Heat Fluid Flow. 2025;35(5):1680–712. doi:10.1108/hff-03-2025-0140.
24. Sohail M, Nazir U, Singh A, Alhushaybari A, Alharthi AM. Morphological applications of triadic hybridized nanoparticles in complex fluid with variable thermal radiations and bouncy force employing the Galerkin finite element method. Numer Heat Transf Part B Fundam. 2025;86(5):1356–73. doi:10.1080/10407790.2024.2312952.
25. Asghar A, Ali Lund L, Shah Z, Vrinceanu N, Deebani W, Shutaywi M. Effect of thermal radiation on three-dimensional magnetized rotating flow of a hybrid nanofluid. Nanomaterials. 2022;12(9):1566. doi:10.3390/nano12091566.
26. Shah SZH, Ayub A, Bhatti S, Khan U, Ishak A, Sherif EM, et al. Aspects of inclined magnetohydrodynamics and heat transfer in a non-Newtonian tri-hybrid bio-nanofluid flow past a wedge-shaped artery utilizing artificial neural network scheme. Z Angew Math Mech. 2024;104(12):e202400278. doi:10.1002/zamm.202400278.
27. Wahid NS, Arifin NM, Khashi'ie NS, Pop I, Bachok N, Hafidzuddin MEH. Unsteady MHD mixed convection flow of a hybrid nanofluid with thermal radiation and convective boundary condition. Chin J Phys. 2022;77:378–92. doi:10.1016/j.cjph.2022.03.013.
28. Abdal S, Siddique I, Afzal S, Chu YM, Ahmadian A, Salahshour S. On development of heat transportation through bioconvection of Maxwell nanofluid flow due to an extendable sheet with radiative heat flux and prescribed surface temperature and prescribed heat flux conditions. Math Meth Appl Sci. 2023;46(10):11355–72. doi:10.1002/mma.7722.
29. Ahmad B, Abbas T, Fatima K, Duraihem FZ, Saleem S. Nonlinear flow of hybrid nanofluid with thermal radiation: a numerical investigation. Z Angew Math Mech. 2024;104:e202200170. doi:10.1002/zamm.202200170.

30. Salahuddin T, Fatima G, Awais M, Khan M. Investigating the stagnation point and Darcy-Forchheimer flow of heat and mass transport with thermal radiation and activation energy. Results Eng. 2023;20:101534. doi:10.1016/j.rineng.2023.101534.
31. Sharma BK, Kumar A, Gandhi R, Bhatti MM, Mishra NK. Entropy generation and thermal radiation analysis of EMHD Jeffrey nanofluid flow: applications in solar energy. Nanomaterials. 2023;13(3):544. doi:10.3390/nano13030544.
32. Rehman MIU, Chen H, Hamid A, Guedri K. Analysis of Cattaneo-Christov heat flux and thermal radiation on Darcy-Forchheimer flow of Reiner-Philippoff fluid. Int J Mod Phys B. 2024;38(3):2450046. doi:10.1142/s0217979224500462.
33. Cross MM. Rheology of non-Newtonian fluids: a new flow equation for pseudoplastic systems. J Colloid Sci. 1965;20(5):417–37. doi:10.1016/0095-8522(65)90022-X.
34. Sahu SK, Shaw S, Thatoi DN, Nayak MK. A thermal management of Darcy-Forchheimer SWCNT-MWCNT Cross hybrid nanofluid flow due to vertical stretched cylinder with and without inertia effects. Waves Random Complex Medium. 2025;35(4):7501–27. doi:10.1080/17455030.2022.2088889.
35. Sajid T, Jamshed W, Eid MR, Cieza Altamirano G, Aslam F, Mahal Alanzi A, et al. Magnetized cross tetra hybrid nanofluid passed a stenosed artery with nonuniform heat source (sink) and thermal radiation: novel tetra hybrid Tiwari and Das nanofluid model. J Magn Magn Mater. 2023;569:170443. doi:10.1016/j.jmmm.2023.170443.
36. Mandal G, Pal D. Estimation of entropy generation and heat transfer of magnetohydrodynamic quadratic radiative Darcy-Forchheimer cross hybrid nanofluid (GO + Ag/kerosene oil) over a stretching sheet. Numer Heat Transf Part A Appl. 2023;84(8):853–76. doi:10.1080/10407782.2022.2163944.
37. Jan A, Mushtaq M, Hussain M. Heat transfer enhancement of forced convection magnetized cross model ternary hybrid nanofluid flow over a stretching cylinder: non-similar analysis. Int J Heat Fluid Flow. 2024;106:109302. doi:10.1016/j.ijheatfluidflow.2024.109302.
38. Farooq U, Liu T, Jan A, Farooq U, Majeed S. Numerical investigation of magnetized bioconvection and heat transfer in a cross-ternary hybrid nanofluid over a stretching cylinder. Multidiscip Model Mater Struct. 2024;20(6):913–36. doi:10.1108/mmms-03-2024-0079.
39. Darvesh A, Collantes Santisteban LJ, Riaz MB, Sánchez-Chero M, Akgül A, Garalleh AL, et al. Inclusion of Hall and Ion slip consequences on inclined magnetized cross hybrid nanofluid over a heated porous cone: spectral relaxation scheme. Results Eng. 2024;22:102206. doi:10.1016/j.rineng.2024.102206.
40. Saleem M, Khouqeer GA, Haq F, Sallah M. Entropy modeling in bioconvective stratified magnetohydrodynamic cross hybrid nanofluid flow with thermal radiation. J Radiat Res Appl Sci. 2025;18(2):101415. doi:10.1016/j.jrras.2025.101415.
41. Hemmat Esfe M. The investigation of effects of temperature and nanoparticles volume fraction on the viscosity of copper oxide-ethylene glycol nanofluids. Period Polytech Chem Eng. 2017;62(1):43–50. doi:10.3311/ppch.9741.
42. Hussain Z, Aljuaydi F, Ayaz M, Islam S. Enhancing thermal efficiency in MHD kerosene oil-based ternary hybrid nanofluid flow over a stretching sheet with convective boundary conditions. Results Eng. 2024;22:102151. doi:10.1016/j.rineng.2024.102151.
43. Rangi RR, Ahmad N. Boundary layer flow past a stretching cylinder and heat transfer with variable thermal conductivity. Appl Math. 2012;3(3):205–9. doi:10.4236/am.2012.33032.